



## Research papers

## Significance of ancient artesian fresh groundwater below the playa of a hypersaline terminal lake of hemispheric significance

Ebenezer Adomako-Mensah<sup>a</sup>, William P. Johnson<sup>a,\*</sup>, Samuel C. Carter<sup>a</sup>, D. Kip Solomon<sup>a</sup>, William D. Mace<sup>a</sup>, Scott A. Hynek<sup>a,b</sup>, Hugh Hurlow<sup>c</sup>

<sup>a</sup> Department of Geology and Geophysics, University of Utah, 115 South 1460 East, Salt Lake City, UT 84112, USA

<sup>b</sup> USGS Utah Water Science Center, 2329 West Orton Circle, West Valley City, UT 84119, USA

<sup>c</sup> Utah Geological Survey, 1594 W North Temple St, Salt Lake City, UT 84116, USA

## ARTICLE INFO

This manuscript was handled by Renato Morbidelli, Editor-in-Chief

## Keywords:

Terminal lakes  
Groundwater  
Playa  
Artesian  
Dust

## ABSTRACT

Terminal lakes world-wide are sensitive to climate, posing air quality degradation to populations adjacent to their drying playas. Great Salt Lake (GSL), the eighth largest terminal lake globally, is proximal to the Salt Lake City metropolitan area, yet the groundwater component of its water budget is relatively unconstrained, as true of terminal lakes globally. Direct measurement of hydraulic parameters and water chemistry were made at GSL's southeastern playa margin in piezometers and retrieved cores to constrain the location and cross-sectional profile of the freshwater-saltwater interface. Groundwater age and recharge elevation were interpreted from tracers analyzed in piezometer samples. Results show that a large body of fresh pressurized groundwater exists underneath a hypersaline lens at depths greater than 9 m below the playa surface, with circular freshwater pipes projecting through the lens in discrete locations. Diffuse upward flow is practically balanced by evapotranspiration demand, and lakeward lateral flux is approximately two orders of magnitude lower than vertical upward flux in the playa. Results demonstrate a mountain-recharge origin with an age since recharge of multiple tens of millennia despite the relatively short lateral distance to the Wasatch Mountain source (20 km), and despite a factor of thousands larger lakeward Darcy flux in the uplands east of the playa. This ancient, pressurized mountain-derived fresh groundwater, while being a relatively minor component of the water budget, may at minimum support mitigation of dust hotspots on the drying playa.

## 1. Introduction

Terminal lakes, as lakes lacking stream outflow, are harbingers of hydroclimatic change worldwide given that for some, their vast surface area-to-depth ratios that render them vulnerable to impacts of increased temperature. Their shrinking footprints expose playa sediment that, when mobilized as dust, can foul air quality for adjacent populations, such as at the Aral Sea of Kazakhstan and Uzbekistan (Wurtsbaugh et al., 2017) and Lake Urmia of Iran (Wurtsbaugh and Sima, 2022). Great Salt Lake, Utah, USA with a surface area of four billion m<sup>2</sup> and an average depth of less than 4 m, has a surface area-to-depth ratio of approximately one billion. Its shrinkage over the past several decades, and its proximity to the Salt Lake City metropolitan area, raise concern for the future air quality for 80 % of Utah's population (approximately 2 million) (Grineski et al., 2024).

GSL is the largest saline lake in the western hemisphere (Conover and

Bell, 2020; Hassibe and Keck, 1991) and is the most studied of twenty terminal lakes in the Great Basin of the western U.S. (Herring et al., 2024), and as such, research regarding GSL's water budget may also inform water budgets of other playa lakes in the western U.S., and globally. Great Salt Lake sits on the eastern edge of the Basin and Range Province, which is characterized by hundreds of north-south trending mountain ranges separated by broad alluvial desert basins that span most of Nevada and parts of Utah, California, Oregon, Idaho, and Arizona (Gardner and Heilweil, 2014). Farmington Bay is one such basin, or structural graben, that is bounded by tectonically active north-south trending normal faults by which the basin has down-dropped relative to structural horsts, or bounding ranges, the Wasatch Mountains on the east and Antelope Island on the west (Fig. 1). The Wasatch Mountains are the easternmost range in the Basin and Range, and the westernmost range in the Rocky Mountains, rising 2,000 m above the valley floor to 3,000 m altitude, exposing rocks ranging from Precambrian to Tertiary

\* Corresponding author.

E-mail address: [william.johnson@utah.edu](mailto:william.johnson@utah.edu) (W.P. Johnson).

in age (Jones et al., 2009). Antelope Island reaches 2,010 m in elevation, and consists of a bedrock core of Archean gneiss, Proterozoic slate and dolomite, and Cambrian quartzite (Mayo and Klauk, 1991).

Characteristic of structural grabens along the Wasatch Front, Farmington Bay has accumulated up to 3,000 m of sediment since the early Tertiary, when these basins formed (Lowe, 2003). The mostly unconsolidated Quaternary basin-fill sediments were deposited by alluvial fans, deltas, and other lacustrine deposits by Pleistocene epoch lakes (Thiros et al., 2010; Manning and Solomon, 2004; Feth et al., 1966). The basin-fill sediments are primarily coarse-grained sands and gravels at the valley margins and become interbedded with finer-grained strata towards the center of the basins. Consequently, aquifers are

largely unconfined near the mountain-block and become increasingly more confined towards the valleys (Thiros et al., 2010; Gillespie et al., 2012, Feth et al., 1966). GSL is the remnant of Lake Bonneville, an ice-age lake that once occupied a significant area of the Basin and Range (Gu et al., 2024). Approximately 13,000–15,000 years ago, following termination of the ice age, GSL assumed its current configuration (Oviatt, 2014).

GSL supports one of the largest and most ecologically important wetland ecosystems in the western United States (Conover and Bell, 2020), with the lake itself harboring a relatively simple ecosystem comprised of invertebrates (brine shrimp and brine flies) and birds, with the surrounding playa and wetlands supporting vegetation, amphibians,

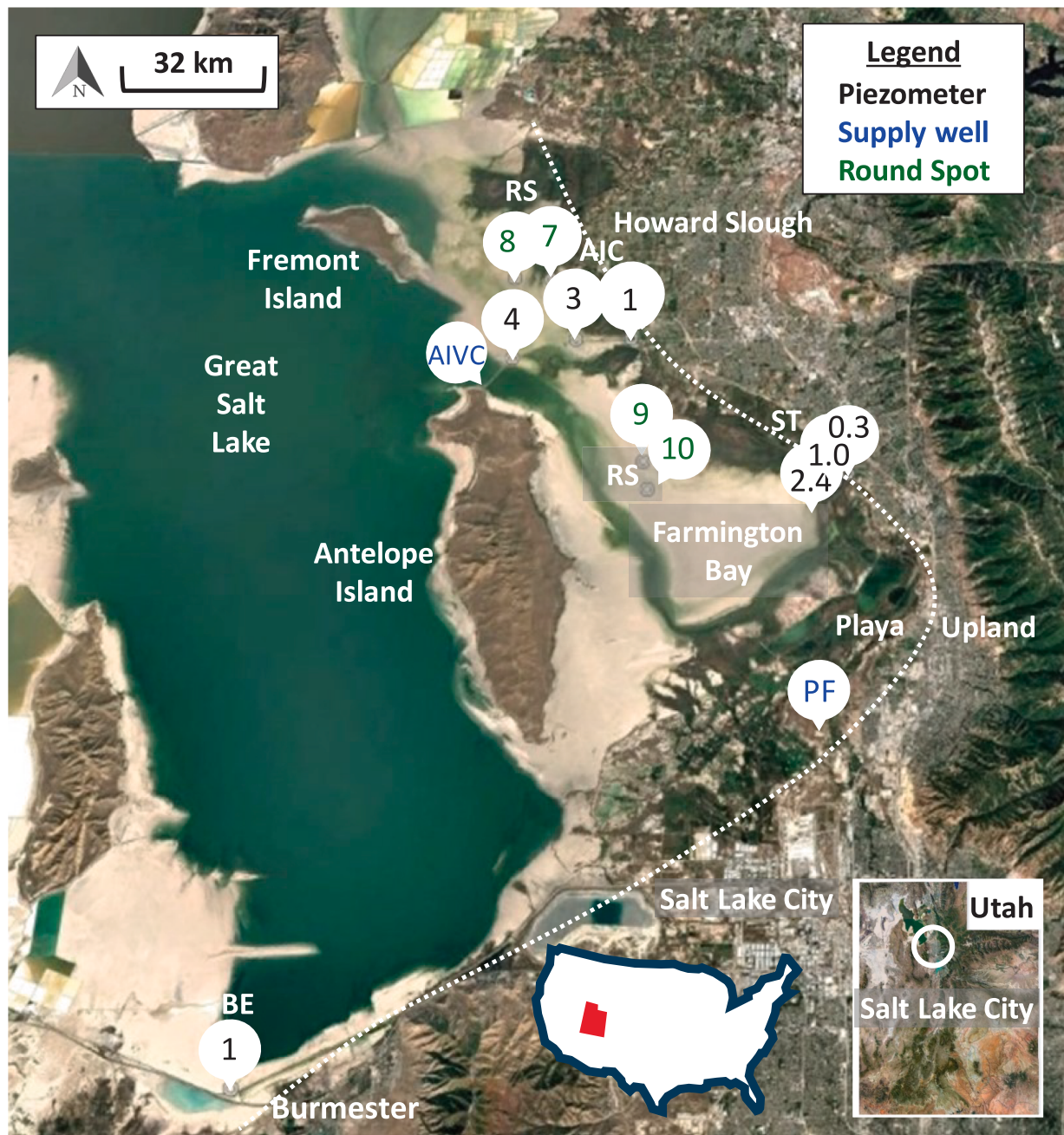


**Fig. 1.** Map of the study area showing locations of nested piezometer sites installed at the eastern and southern shores of Great Salt Lake (GSL) at four areas: a) the northern boundary of Farmington Bay (AIC transect), b) the southeastern margin of Farmington Bay (ST transect), c) the southern shore of GSL 17 km SW of the Saltair Marina (BE1), and d) at select “round spots” (RS), several tens of which are visible via Google Earth on the central playa of Farmington Bay (RS9 and RS10) and in the area lying east of Fremont Island and west of Howard Slough (RS7 and RS8). Locations of two supply wells for the Antelope Island visitor's center (AIVC) and the Peterson Family (PF) are shown at the north and south boundaries, respectively, of Farmington Bay.

reptiles, and mammals (Conover and Bell, 2020; Tavernia et al., 2021; Johnson et al., 2019). The Western Hemisphere Shorebird Reserve Network recognizes GSL as a habitat of hemispheric importance for millions of migratory birds. As part of the Pacific Flyway, GSL provides critical habitat for 12 million migratory birds annually, representing 339 bird species (Wilson, 2010), and underpins regional economies contributing an estimated \$1.9 billion annually through industries such as mineral extraction, recreation, and brine shrimp harvest (Wurtsbaugh et al., 2016).

GSL's surface elevation has trended downward since 1987, and in 2022, the lake dropped to a record low elevation of 4,188.6 ft, the lowest recorded level (Great Salt Lake Strike Team, 2025). As a terminal lake, the only outflows from GSL are evaporation and brine extraction (Johnson et al., 2019), and surface inflows to GSL are primarily from the Bear, Weber, and Jordan Rivers, which drain the surrounding Uinta and Wasatch mountains and flow into the southern arm of the lake (Jones et al., 2009).

Direct precipitation is another significant surface inflow, accounting for approximately 30 % of the water budget (Hall et al., 2021). Preceding estimates of groundwater discharge to GSL as derived from water budget residuals suggested that approximately 3 % of inflow to GSL is from groundwater (Waddell and Barton, 1980). Subsequent studies including stream chemistry analyses (Godsey et al., 2009), groundwater modeling (Masbruch et al., 2016), streamflow modeling (Brooks et al., 2021), and stream hydrograph analysis (Wolf et al., 2023) all suggest that the amount of groundwater entering GSL either directly or via seepage into tributaries upstream has been underestimated. Recent studies suggest that groundwater seepage accounts for approximately 10 %–12 % of total inflows to GSL, as determined from geochemical modelling (Bunce et al., 2025), and application of Darcy's Law in a geospatial analysis (Zamora and Inkenbrandt, 2024).

The above studies highlight discrepancies regarding groundwater inflow to GSL, and highlight the lack of, and the need for, direct measurements of groundwater inflows to GSL. Furthermore, the location and cross-sectional profile of the freshwater-saltwater interface at the margin of GSL has not been previously described. This paper describes direct measurements of hydraulic head, hydraulic conductivity, and water chemistry from piezometers installed in, and sediment cores retrieved from, the southeast playa margin of GSL. Interpretations made from water chemistry included spatial trends in major ion composition, light stable isotope signatures, groundwater age, and recharge elevation.

## 2. Methods

### 2.1. Study area

Fifty-six nested piezometers with screen depths ranging from 33 m to 1.5 m were installed at four locations at the eastern and southern shores of Great Salt Lake (GSL) (Fig. 1 and Tables SI-1 to SI-4): a) the northern boundary of Farmington Bay at the Antelope Island Causeway (AIC transect), b) the south transect at the southeastern margin of Farmington Bay (ST transect), c) the southern shore of GSL 17 km SW of the Saltair Marina east of Burmester (BE1), and d) at select “round spots” (RS), several tens of which are visible via Google Earth on the central playa of Farmington Bay (RS9 and RS10) and in the area lying east of Fremont Island and west of Howard Slough (RS7 and RS8).

The AIC and ST transects are oriented east–west, each having nested piezometers at three sites spanning the north boundary of Farmington Bay (AIC sites 1, 3, and 4 from east to west) spanning the eastern-most playa margin (ST sites 0.3, 1.0, and 2.4 from east to west) (Fig. 1). Supply wells for the Antelope Island visitor's center (AIVC) and for the Peterson Family (PF), at the north and south boundaries, respectively, of Farmington Bay (Fig. 1) had screen depths ranging from approximately 122 m (400 ft) to 213 m (700 ft).

### 2.2. Piezometer installation

Deep piezometers, with depths greater than or equal to 9.1 m (30 ft) were installed using a Geoprobe direct push rig (E.T. Technologies Inc.). Each piezometer consisted of a 1.9-cm (0.75 in) inner diameter PVC pipe and a 0.76 m (2.5 ft) length screen pre-packed with medium-grained sand. The top 0.61 m (2 ft) was sealed using hydrated bentonite chips (Adomako-Mensah, 2025).

Sediment cores were collected at various depths from select sites along the AIC transect and at site ST0.3 and site BE1. Sediment cores were collected at depths ranging from 9.1 m (30 ft) to 30.5 m (100 ft) from select sites along the AIC transect and at site ST0.3 and site BE1. These depths were chosen within the bounds of the geoprobe capabilities to evaluate correspondence of pore water properties at greater vertical resolution relative to piezometer samples. Cores were sealed after collection and stored at 4 °C in the Geology and Geophysics cold room at the University of Utah. Pore water was extracted from the cores using Rhizon samplers (Rhizosphere™) attached to disposable syringes that were extended using aluminum spacers to produce vacuum. Samplers were inserted at 0.3 m–1.5 m (1 ft–5 ft) depth intervals and left under vacuum for 24 hrs. The extracted sample volumes ranged from 0.1 mL to 20 mL. Specific conductance (SpC) was measured using a conductivity meter (Jenway 4510), capable of analyzing samples as small as 1 mL. A standard calibration curve was developed using known standards, and error bars were determined based on the standard deviation of readings from the known standards. Additional analyses performed on the extracted pore water measured major ions, trace elements,  $\delta^{2}H$  and  $\delta^{18}O$ , as described below.

Shallow piezometers, with depths less than 9.1 m (30 ft), were installed using an electric jackhammer to drive stainless-steel cylinders (1.5 cm diameter) with disposable stainless-steel points, within which PVC pipes (1.3 cm, 0.5 in inner diameter) with a 0.3 m (1 ft) length slotted screen. The top 0.61 m (2 ft) was sealed using hydrated bentonite chips.

Additional shallow piezometers, with depths less than 5 m (15 ft), were installed by hand augur (6.4 cm, 2.5 in diameter), into which PVC pipe (5.1 cm, 2 in inner diameter), with a 21-cm (8.3 in) length slotted screen (Adomako-Mensah, 2025). The bottom of the pipe was sealed with a 5.1-cm (2 in) diameter PVC plug using CCW Universal Single-Ply Sealant. Excavated clay material was repacked into the uppermost 0.3 m (1 ft), and the top was sealed with hydrated bentonite chips.

### 2.3. Hydraulic conductivity

Horizontal hydraulic conductivity ( $K_h$ ) was estimated from slug tests performed in piezometers at several sites. Each test involved measuring the static water level with a level meter (In-Situ, Inc.), then removing groundwater from the piezometer using a Waterra pump and recording the water-level recovery with time (Adomako-Mensah, 2025). Horizontal hydraulic conductivity was calculated using the Hvorslev (1951) method, assuming that the rate of inflow to the well is proportional to the hydraulic conductivity of the surrounding formation:

$$Q(t) = A \frac{\partial h}{\partial t} = FK\{H - h(t)\} \quad (1)$$

where  $Q(t)$  is the volumetric flow into a piezometer of cross-sectional area  $A$  with change in hydraulic head over time  $dh/dt$ , being calculable from a shape factor  $F$  dependent construction details of the piezometer, and where  $K$  is the hydraulic conductivity within the piezometer's radius of influence,  $H$  is the static water level, and  $h(t)$  is the time-dependent hydraulic head within the piezometer. For a well screen interval of length  $L$  in a uniform soil, the shape factor  $F$  is calculated from:

$$F = \frac{2\pi}{\ln \left[ \frac{mL}{D} + \sqrt{1 + \left( \frac{mL}{D} \right)^2} \right]} \quad (2)$$

where  $D$  is the outer casing diameter, and  $m$  is the transformation factor defined as:

$$m = \sqrt{\frac{K_h}{K_v}} \quad (3)$$

where  $K_h$  was assumed to be three times greater than the vertical hydraulic conductivity ( $K_v$ ).

$K_h$  was then calculated from the equation below developed from Eqs. (1)–(3) (Hvorslev, 1951):

$$K_h = \frac{d^2 \ln \left[ \frac{mL}{D} + \sqrt{1 + \left( \frac{mL}{D} \right)^2} \right]}{8LT_o} \quad (4)$$

where  $d$  is the inner casing diameter and  $T_o$  is the basic time lag.

Vertical hydraulic conductivity ( $K_v$ ) was estimated from laboratory column tests on sediment cores that were maintained under saturated conditions following removal. For each core, one 2-cm segment was removed from each of the twelve (AIC3) or six (RS9) 1.5-m length cores comprising the total retrieved cores from the AIC3 (18 m) and RS9 (9 m) sites. A falling-head permeameter method was used because the low hydraulic conductivity of the cores is generally small making constant head tests difficult. Each test used a sediment core of 5-cm length and 1.6-cm radius wrapped in heat-shrink tubing that was then placed in an acrylic tube and wrapped in electrical tape (Figure SI-9). The bottom end of the sediment core was then submerged in a water reservoir to set a constant hydraulic head at the core outlet. An amplifier tube of 0.2-cm radius attached to the core inlet (top) was filled with water using a syringe to induce downward flow through the core. The change in water level over time ( $t$ ) was measured, with initial head ( $h_1$ ) and final head ( $h_2$ ) recorded.  $K_v$  was then calculated using the falling-head equation:

$$K_v = \frac{r^2 L}{R^2 t} \ln \left( \frac{h_1}{h_2} \right) \quad (5)$$

Rhodamine dye was added to the amplifier tube water to allow post-measurement visual confirmation that flow occurred in the core interior rather than the annulus. Grain size analyses of sediment were performed using a laser diffractometer (Sympatec, Inc.); sediment representing sand and clay end members to confirm grain size estimates from hand-texture method (Figure SI-7).

#### 2.4. Hydraulic head

Hydraulic heads were determined from water levels in piezometers as described below. Relative elevations of piezometers at each site were determined using differential leveling using an automatic level with an accuracy of  $\pm 2$  mm. Because site elevations were within 1.5 m of one another across all sites, hydraulic heads comparison across sites was allowed using site elevations determined from Google Earth.

Artesian piezometers (all of which exceeded 18 m depth) were equipped with compressible packers (Aardvark Packers, LLC.) below which non-vented pressure transducers (Aqua Troll 200 and 400, In-Situ, Inc.) were installed. Pressure readings were converted to height of water ( $D$ ) in meters above the transducer using the relationship below, which corrects measured pressure in psi ( $P_m$ ) for barometric pressure in psi ( $B_m$ ) since  $P_m$  is combined water and atmospheric pressure:

$$D = \frac{0.703073(P_m - B_m)}{SG} \quad (6)$$

where  $SG$  is the specific gravity of the groundwater.

Water level elevation was then obtained by adding the deployed transducer elevation (reference point) to  $D$ .

For non-flowing intermediate depth piezometers (depths between approximately 5 m and 18 m), no packers were used, and vented pressure transducers (Aqua Troll 200 and 400, In-Situ, Inc.) were installed, for which pressure readings in psi ( $P$ ) were converted to  $D$  in meters using:

$$D = \frac{0.703073(P)}{SG} \quad (7)$$

For shallow depth piezometers (depths less than 5 m), non-vented pressure transducers (Rugged Troll 100, In-Situ, Inc.) were installed, for which pressure readings ( $P_m$ ) in psi were corrected according to Eq. (6). Hydraulic head was corrected for the variable-density groundwater to obtain an equivalent freshwater hydraulic head ( $h_f$ ) following (Woessner and Poeter, 2020):

$$h_f = z_i + (h_i - z_i) \frac{\rho_s}{\rho_f} \quad (8)$$

where  $z_i$  is the midscreen elevation of the piezometer,  $h_i$  is the water level elevation,  $\rho_s$  is the average groundwater density across each season, and  $\rho_f$  is the density of freshwater. Lateral hydraulic gradients were then calculated using the freshwater head correction. Vertical hydraulic gradient was further corrected for buoyancy arising from vertical density differences. The buoyancy term is made up of the mean groundwater density ( $\rho_{mean}$ ) between two piezometers and  $\rho_f$ . The mean density was obtained by integrating the density values over the vertical distance ( $\Delta z$ ) using the bisection method. The buoyancy-corrected vertical hydraulic gradient was then calculated as (Post and Simmons, 2021):

$$\frac{dH}{dL} = \frac{\Delta h_f}{\Delta z} + \frac{\rho_{mean} - \rho_f}{\rho_f} \quad (9)$$

where  $\Delta h_f/\Delta z$  is the freshwater head gradient.

#### 2.5. Field parameters

Groundwater temperature and pressure were measured using Aqua Troll 200 and 400 pressure transducers (In-Situ, Inc) that were calibrated before measurements (Adomako-Mensah, 2025). Additionally, the Aqua Troll 200 probes measured SpC ( $\mu\text{s}/\text{cm}$ ), which was converted to salinity ( $\text{mg/L}$ ) using a conversion factor ( $k$ ) as follows:

$$\text{Salinity} = k \times \text{SpC} \quad (10)$$

where  $k$  is dependent on the type of water (i.e., predominance of monovalent versus divalent major ions), and salinity (Hem, 1985). This is generalized as  $k$  values equal to 0.47–0.50 (Eutech Instruments, 1997) in fresh water, and  $k$  values equal to 0.7–1.0 in seawater to hypersaline water, respectively (Ponce, 2014). Groundwater density was calculated from salinity and temperature measured by Aqua Troll 200 transducer (In-Situ, Inc.) using Standard Method 2520 C (Rice et al., 2017).

#### 2.6. Sampling for laboratory analyses

Groundwater samples were collected from piezometers to be analyzed for major ions, radioactive and stable isotopes ( ${}^3\text{H}$ ,  ${}^{14}\text{C}$ ,  ${}^{13}\text{C}$ ,  $\delta {}^2\text{H}$ ,  $\delta {}^{18}\text{O}$ ), and dissolved noble gases ( ${}^3\text{He}$ ,  ${}^4\text{He}$ ,  ${}^{20}\text{Ne}$ ,  ${}^{40}\text{Ar}$ ,  ${}^{84}\text{Kr}$ ,  ${}^{129}\text{Xe}$ ). The AIVC and PF supply wells were sampled solely for  ${}^{14}\text{C}$  and  ${}^3\text{H}$  age and dissolved gases, as described below. Piezometers were purged three times and allowed to recover before sampling, and all sample bottles were rinsed three times with the groundwater before sample collection. Major ion samples were collected using a peristaltic pump (Geotech Environmental Equipment, Inc.) and pumped through an in-line 0.45  $\mu\text{m}$  cartridge filter into a low-density polyethylene (LDPE) 20 mL bottle,

acid rinsed in 10 % HCl (Adomako-Mensah, 2025). Stable isotope samples ( $\delta^2\text{H}$ ,  $\delta^{18}\text{O}$ ) were collected using the same pumping method as for major ions. Samples were stored in 1.5 mL glass vials (Adomako-Mensah, 2025). To estimate groundwater ages,  ${}^3\text{H}$  and  ${}^{14}\text{C}$  samples were collected for analysis. Tritium ( ${}^3\text{H}$ ) was used to provide information on modern recharge (decadal timescales), whereas radiocarbon ( ${}^{14}\text{C}$ ) was used to constrain older groundwater (centuries to millennia).  ${}^3\text{H}$  samples were collected in 500 mL Nalgene® plastic bottles with minimal headspace and tightly sealed.  ${}^{14}\text{C}$  samples were collected in 1 L glass bottles, filled from bottom up, and displacing three bottle volumes before capping tightly. To estimate the elevation and temperature at which groundwater recharge occurred, samples were collected for dissolved noble gas analysis. Dissolved gas samples were collected via peristaltic pump in copper tubes with custom-fabricated one-way valves attached to Teflon tubing. After passing at least several copper tube volumes, the bottom end of the copper tube was clamped while reversing the pump to maintain pressure, after which the upper end of the copper tube was clamped.

## 2.7. Laboratory analyses

Major ion concentrations were measured at the ICP-MS Metals and Strontium Isotope Facility at the University of Utah. Water type was determined from major ion concentrations and alkalinity using trilinear diagrams (Figure SI-8). Stable isotopes ( $\delta^2\text{H}$ ,  $\delta^{18}\text{O}$ ) were analyzed at the SIRFER laboratory after vacuum distillation in the Dissolved Gas Lab at the University of Utah. These isotopes provide insight into the evaporative history of groundwater. Partial evaporation results in isotopic enrichment along an evaporation line that diverges from the Local Meteoric Water Line (LMWL) (Bowen et al., 2018). Tritium ( ${}^3\text{H}$ ) concentrations were measured at the Dissolved Gas Lab at the University of Utah. Groundwater age was estimated using the  ${}^3\text{H}/{}^3\text{He}$  method, which relies on the decay of  ${}^3\text{H}$  to  ${}^3\text{He}$ . Background atmospheric  ${}^3\text{H}$  ranges between 6 and 8 TU (Thiros and Manning, 2004), while concentrations below 0.1 TU indicate groundwater older than 85 years (Carter, 2025). Initial tritium concentrations were reconstructed from measured  ${}^3\text{H}$  and

interpreted  ${}^3\text{He}$  values and compared with historical atmospheric records (Michel et al., 2018).  ${}^{14}\text{C}$  samples from the AIC piezometers were collected by the USGS and analyzed by National Ocean Sciences Accelerator Mass Spectrometry facility at Woods Hole Oceanographic Institution (NOSAMS). The data is publicly available from the Water Quality Portal (2021).  ${}^{14}\text{C}$  samples from PF and RS9 were analyzed by the University of Georgia Center for Applied Isotope Studies. Radio-carbon data served as a qualitative indicator of groundwater age.

Dissolved noble gases are chemically inert and reflect the temperature, pressure, and salinity of recharge conditions (Aeschbach-Hertig and Solomon, 2013). The closed-system equilibration (CE) model which accounted for excess air and fractionation was used to interpret noble gas concentrations and compute a range of possible recharge temperatures and elevations. A local recharge elevation-temperature relationship was then used to determine the most probable recharge temperature and elevation (Carter, 2025).

Recharge temperature and elevation were calculated using a weighted least squares inversion method that minimize the error-weighted deviation between measured and modeled noble gas concentrations using a local recharge elevation-temperature relationship (Carter, 2025).

## 3. Results

### 3.1. Hydraulic heads

Hydraulic heads were higher in deeper piezometers across the AIC transect (Fig. 2), with the steepest gradients being predominantly vertical, demonstrating a strong upward hydraulic gradient across the north boundary of Farmington Bay. Lateral hydraulic gradients were relatively modest (Fig. 2), and were westward at the eastern margin, and eastward at the western margin. The eastward lateral gradient at the westward margin might reflect increased stage in Farmington Bay channel due to snowmelt runoff in Spring 2025 and engineered release of flow from upstream Utah Lake in Fall 2024. However, increased stage of Farmington Bay channel would be expected to impact shallow rather than

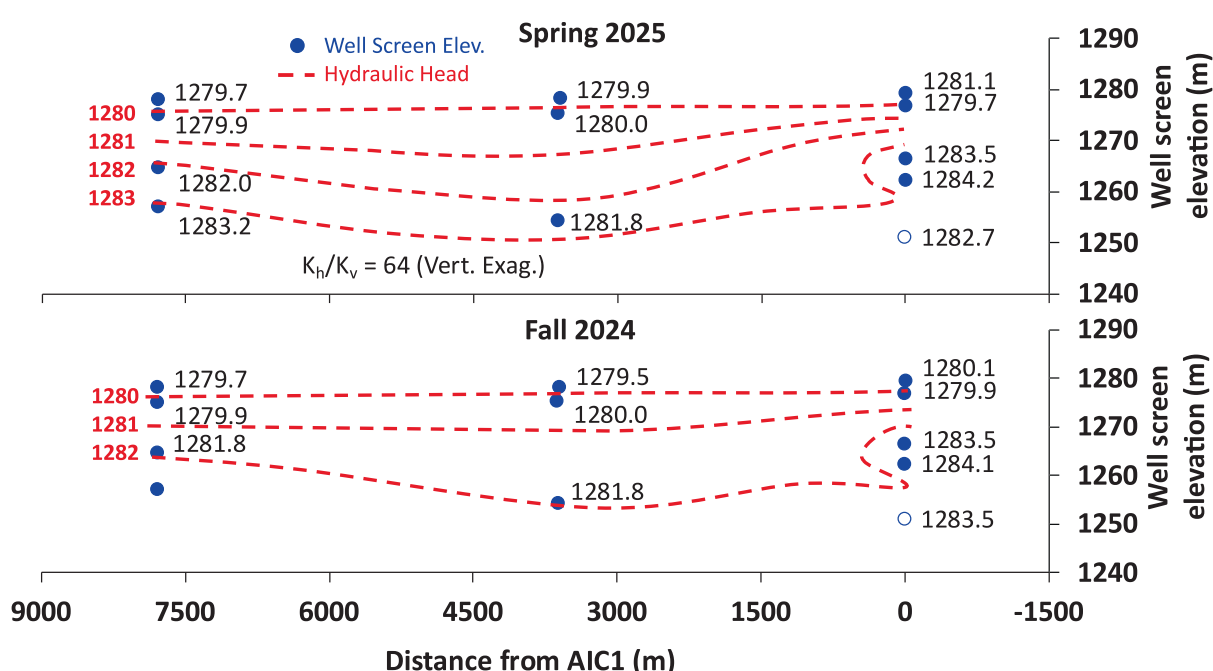


**Fig. 2.** Cross-sectional plot of contoured (dash red lines) freshwater equivalent hydraulic heads measured in piezometers at AIC (closed blue circles). Numeric labels on plot are hydraulic head values in meters. Open blue symbol depicts value at AIC1-30.5 (30.5 m depth) which showed continuous groundwater leakage via the well annulus. Spring 2025 and Fall 2024 values shown in top and bottom panels, respectively. A vertical exaggeration of 64 was used in accordance with a  $K_h/K_v$  ratio of 64. (For interpretation of the references to colour in this figure legend, the reader is referred to the web version of this article.)

deep hydraulic heads, suggesting that the eastward lateral gradient might reflect eastward groundwater flux from the east flank of Antelope Island.

Time series plots of hydraulic heads at all four areas (Figure SI-1) show that a strong upward hydraulic gradient existed across the entire south-east margin of GSL across the duration of the study, particularly at RS9 and episodically at ST0.3–33.1, which showed step variation (Figure SI-1, dark blue triangles) that likely reflected episodic leakage around the packer, with upper values presumably reflecting actual hydraulic head. Hydraulic heads decreased during summer months particularly in shallow wells (Figure SI-1), with an abrupt hydraulic head increase in the 1.5 m piezometer at AIC3 corresponding to a 2.4-inch rain event on October 4, 2025 (Figure SI-1) that also manifested as damped increases in the piezometers at mid and shallow depths at RS9. Exceptions to the relative temporal constancy of deeper hydraulic heads include the overall decreasing hydraulic head in AIC1-30.5 (Figure SI-1, dark blue triangles) due to upward flow through the annulus between the well casing and surrounding sediment, as well as

the large variability in AIC3-25.9 (Figure SI-1, dark blue circles) after mid-October due to gas pressure buildup below the packer used to seal the well above the pressure transducer. Hydraulic head in the shallow well at BE1 was impacted by gas pressure buildup below the packer, and so was not included in the analysis. Overall, the hydraulic head data indicates greater hydraulic heads in deeper piezometers by as much as approximately 10 m at the central and southeast sites of Farmington Bay (ST0.3 and RS9), and by approximately 2 m at the AIC transect (Figure SI-1).

Upward vertical hydraulic gradients were relatively temporally constant and generally ranged up to 0.6, with RS9 being a notable exception with an upward hydraulic gradient of approximately 1.8 (Figures SI-1, SI-2). Vertical hydraulic gradients in the AIC transect decreased westward toward GSL (Figures SI-1, SI-2), as shown in upward hydraulic gradients that decreased successively from AIC1 (triangles) to AIC3 (circles) to AIC4 (squares). Shallow vertical hydraulic gradients showed greater temporal variability with lower hydraulic head during the summer season (Figures SI-1 and SI-2). Shallow vertical

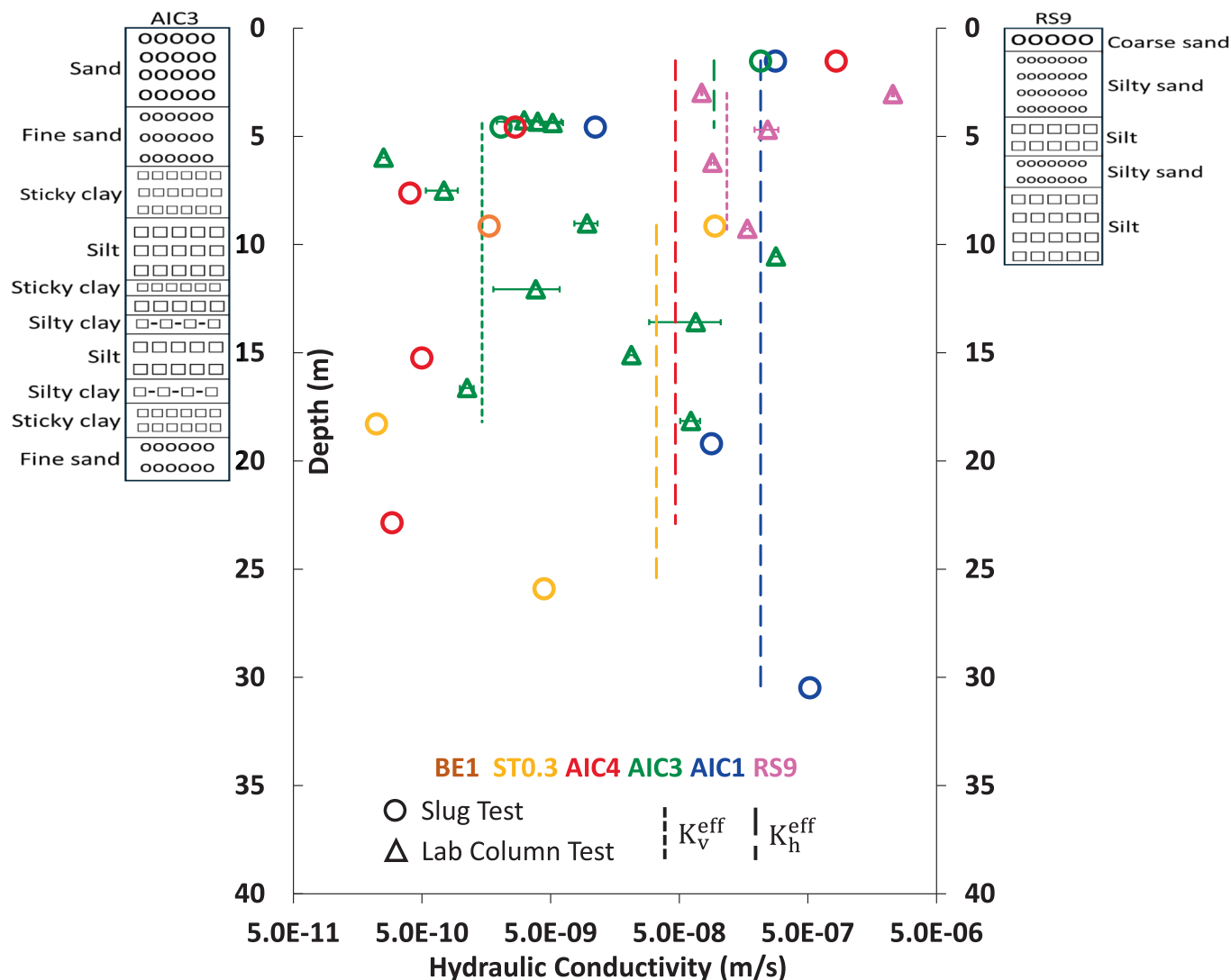


**Fig. 3.** Hydraulic conductivities from slug tests (horizontal) and laboratory column tests (vertical) as a function of well screen depth (m) from slug tests or core sample depth (m) from column tests. Schematic stratigraphic sections of cores from AIC3 and RS9 are shown to the left and right of the hydraulic conductivities, respectively. Horizontal hydraulic conductivities from slug tests and vertical hydraulic conductivities from laboratory column tests are denoted by circles and triangles, respectively. The different sites are denoted by colors. The effective (thickness-weighted harmonic mean) vertical hydraulic conductivity ( $K_v^{\text{eff}}$ ) and the effective (thickness-weighted geometric mean) horizontal hydraulic conductivity ( $K_h^{\text{eff}}$ ) are denoted by fine and coarse dashed lines, respectively. Error bars represent standard deviations of triplicate measurements on core segments. (For interpretation of the references to colour in this figure legend, the reader is referred to the web version of this article.)

hydraulic gradients were in some cases downward (Figures SI-1 and SI-2).

Lateral hydraulic gradients were more than two orders of magnitude lower than vertical hydraulic gradients (Figures SI-2 versus SI-3). Temporal variation in lateral hydraulic gradient was greater at the southeastern area of Farmington Bay (ST) than at the northern boundary of Farmington Bay (AIC) (Figure SI-3, right versus left panels). Lateral hydraulic head gradients indicate that flow is predominantly westward at both the AIC and ST transects, except for the western segment at AIC (3–4) during summer, and the eastern segment at ST (0.3–1.0) during summer and fall (Figure SI-3). In contrast, at ST a spatially consistent westward lateral gradient existed during winter and spring (Figure SI-3, right panel). Westward lateral gradients decreased from east to west at AIC (Figure SI-3, left panel, triangles to squares) more so for the deep versus shallow piezometers (Figure SI-3, blue versus red symbols). The magnitude of the winter-spring westward lateral gradient at ST also decreased westward (Figure SI-3). During summer and fall, this lateral hydraulic gradient at ST decreased in both direction from the transect center (Site 1.0) due to a relatively constant hydraulic head at that location.

### 3.2. Hydraulic conductivities

Across the AIC sites, horizontal hydraulic conductivity ( $K_h$ ) from slug tests generally decreased from east to west (toward GSL) (Fig. 3, circles), where cooler and warmer colors denote eastern and western sites, respectively, in the AIC transect. Effective (thickness-weighted geometric mean) horizontal hydraulic conductivity ( $K_h^{eff}$ ) values were higher at eastern site AIC1 (2.15E-7 m/s) relative to western site AIC4 (4.67E-8 m/s) (Fig. 3, vertical coarse dashed lines). Limited slug test measurements at ST0.3 produced a three order-of-magnitude range in  $K_h$  (from 2.2E-10 m/s to 9.5E-8 m/s). The single slug test at BE1 produced a  $K_h$  value at the low end of this range (1.7E-9 m/s).

Vertical hydraulic conductivity ( $K_v$ ) values measured in laboratory column tests for AIC3 cores produced  $K_v$  values that were lowest in clayey units, and highest in sandy units (Fig. 3, green triangles and stratigraphic columns). Effective (thickness-weighted harmonic mean) vertical hydraulic conductivity ( $K_v^{eff}$ ) at AIC3 was 1.5E-9 m/s ± 8.1E-11 m/s (6 % relative error), where the standard error was determined via error propagation of standard deviation of triplicate

measurements on core segments (Fig. 3, vertical fine dashed lines). This  $K_v^{eff}$  value from AIC3 is approximately two orders of magnitude smaller than the  $K_h^{eff}$  (9.3E-8 m/s) at the same site (Fig. 3).

Values of  $K_v$  measured for site Round Spot 9 (Fig. 3) ranged from 7.5E-7 m/s to 2.3E-6 m/s, with a thickness-weighted harmonic mean of 1.2E-7 m/s ± 3.7E-09 m/s (3 % relative error). This  $K_v^{eff}$  is approximately two orders of magnitude greater than that for the playa at AIC3 (1.5E-9 m/s), suggesting that the round spots in the playa are associated with higher permeability sediment in addition to higher upward hydraulic gradient (Figures SI-1 and SI-2). The origin of these subsurface structures warrants further investigation.

### 3.3. SpC profiles

Pore water SpC profiles from collected cores showed SpC maxima at approximately 3 m to 4 m (10 ft–13 ft) depths, with upward-decreasing values reflecting surface inflow from precipitation and snowmelt (Fig. 4). That peak pore water SpC values approach those in GSL, and pore water type (NaCl) matches GSL water type, as described below, indicate that periodic GSL inundation drove elevated shallow groundwater salinity beneath the playa. Decreased SpC at depths above the SpC peak may be driven by freshwater inundation during high bay stands (runoff), in addition to snowmelt and precipitation, as indicated by downward vertical hydraulic gradients (Figure SI-3) in shallow wells during the April–May months (snowmelt season). SpC decreased with depth below the SpC peak to freshwater values at approximately 9 m (30 ft) depth at the AIC and ST transects, and somewhat deeper at the BE1 site, approximately 15 m (50 ft) (Fig. 4).

Applying  $K_v^{eff}$  to the observed downward hydraulic gradient at AIC1 produces a downward velocity of 1.3E-2 m/year, or a 0.013 m annual downward translation of the peak salinity during the snowmelt and runoff season, which is comparable to the upward annual translation (0.03 m) via the upward velocity (2.6E-3 m/year), as developed below. As such, the location of the salinity peak likely reflects a balance of upward translation from below and downward translation from above, although periodic inundation during elevated GSL stages, ETr, and spatial variability of runoff add complexity that is not represented in this simple analysis.

At the AIC transect, SpC peaks increased westward towards GSL (Fig. 4) where the east-to-west progression is denoted by cool to warm

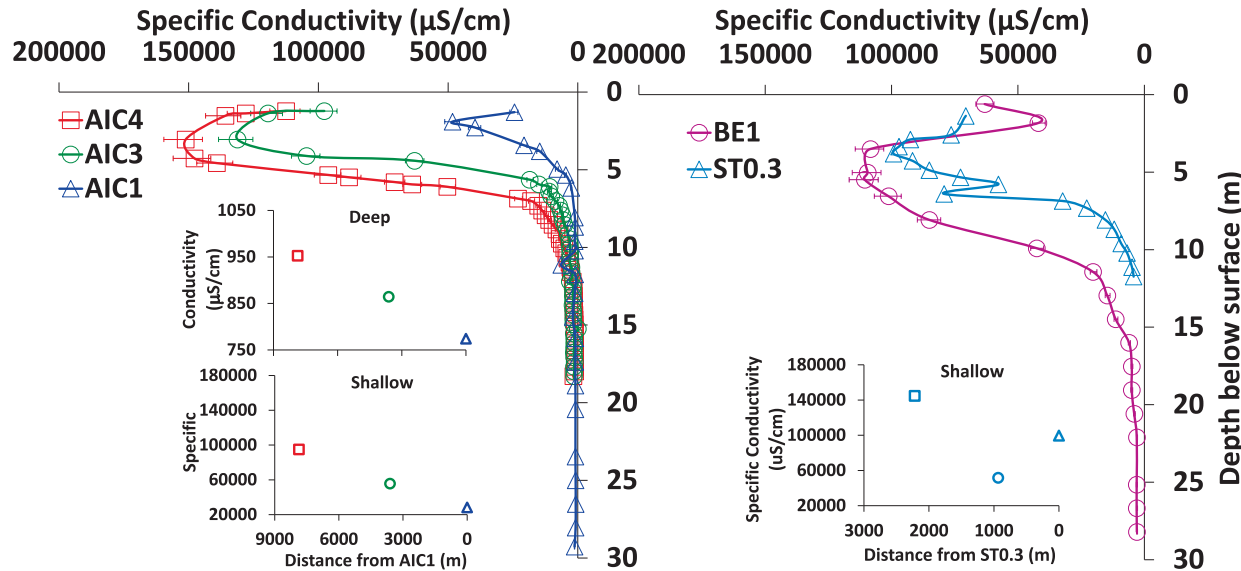


Fig. 4. SpC profile from cores collected from the AIC transect (left panel), ST0.3 and BE1 sites (right panel). Insets show measured SpC from deep piezometers (depth exceeding approximately 18 m) and shallow piezometers (depths less than 5 m) at the AIC and ST transects.

symbol colors, respectively. That peak salinity increases westward (with increased proximity to the Farmington Bay channel) likely reflects greater depths and/or frequencies of inundation by hypersaline water during higher GSL elevations that inundate Farmington Bay. Piezometer groundwater salinities also demonstrate the hypersaline-to-freshwater transition across a 9 m depth from the surface (Fig. 4), and as described below.

### 3.4. Windows into the fresh groundwater resource (round spots, mystery island, phragmites oases)

Circular features that dot the playa referred to as “round spots” (RS) show specific conductivities in their centers corresponding to freshwater at all depths including surface, as shown for RS9 (Fig. 5), center (blue) profile. From the center to the edge of Round Spot 9, i.e., corresponding to blue to red profiles in Fig. 5, near surface groundwater transitions from fresh to hypersaline. These discrete “pipes” of groundwater inflow correspond to greater hydraulic conductivities (Fig. 3). Electrical resistivity surveys showed high resistivity groundwater (freshwater) at all depths in the round spot center, and hypersaline groundwater at shallow depths at the round spot edge (Michael Thorne, personal communication), matching SpC measurements in the piezometers (Fig. 5).

Measured SpC at round spot centers more generally were inversely related to round spot radius (Fig. 6), with larger round spots showing lower SpC, and smaller round spots showing higher SpC. Given that four out of four round spots investigated showed the above-described characteristic, we presume that the many other round spots also show this characteristic. RS7 and RS8 are small relative to other round spots in the northeastern playa of GSL (Figs. 1 and 6). The presence of round spots on the northeastern GSL playa indicates that freshwater exists at depth under the entire eastern GSL playa. This is corroborated by ground-based electrical resistivity surveys on the northeastern playa (Michael Thorne, personal communication).

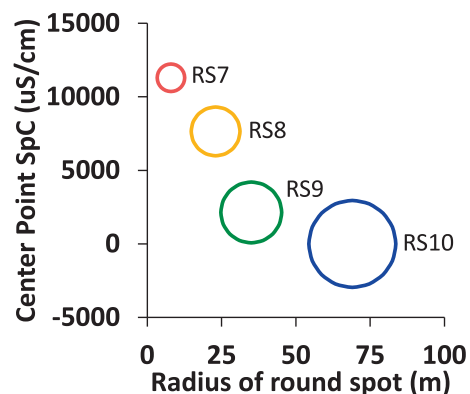


**Fig. 6.** Bubble plot showing the relationship between round spot radius (bubble size) and center point specific conductance (SpC) at approximately 2 m depth. The freshwater to brackish continuum is represented by the ramp from cool to warm colors, respectively. (For interpretation of the references to colour in this figure legend, the reader is referred to the web version of this article.)

### 3.5. Water chemistry (age, recharge elevation, water type, SpC, stable isotope signatures)

Groundwater ages range from several tens-of-decades in shallow groundwater to multiple millennia in deep groundwater according to  $^{3}\text{H}/^{3}\text{He}$  ratios in the former, and percent modern carbon (pMC) values measured on alkalinity in the latter, ranging from 16.2 to 0.7 (Fig. 7, top left panel). Ancient deeper groundwater exists at the surface at round spots such as RS9 (Fig. 7, top left panel) where this water is “piped” upwards from depth. Recharge elevations increased modestly with depth, except for site RS9A (center of RS9), which showed higher recharge elevation at shallow depth (Fig. 7, top right panel), as expected

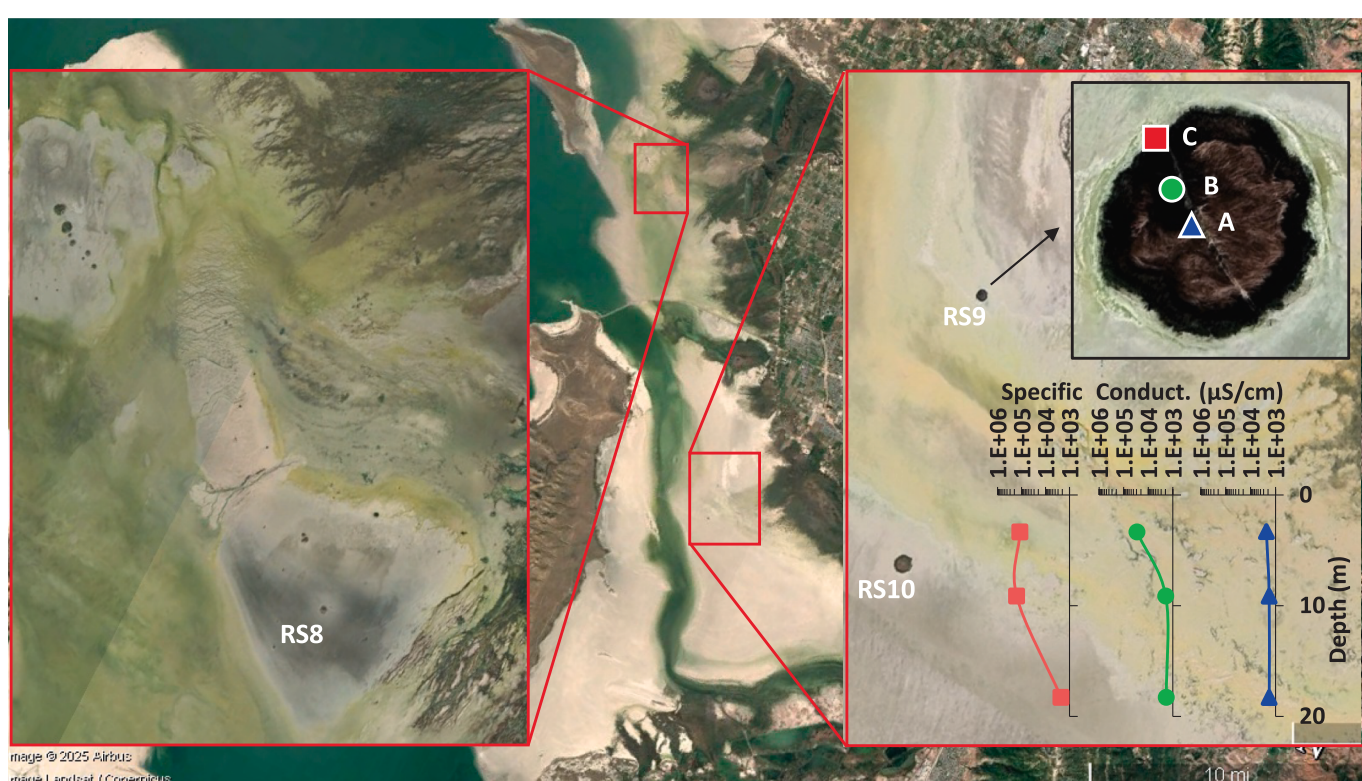


**Fig. 5.** Map of RS8 (left panel), RS9 and RS10 (right panel) showing locations of piezometer pairs and measured specific conductivities at RS9. The freshwater to hypersaline from the center to the edge of Round Spot 9 are shown with cool to warm symbol colors. (For interpretation of the references to colour in this figure legend, the reader is referred to the web version of this article.)

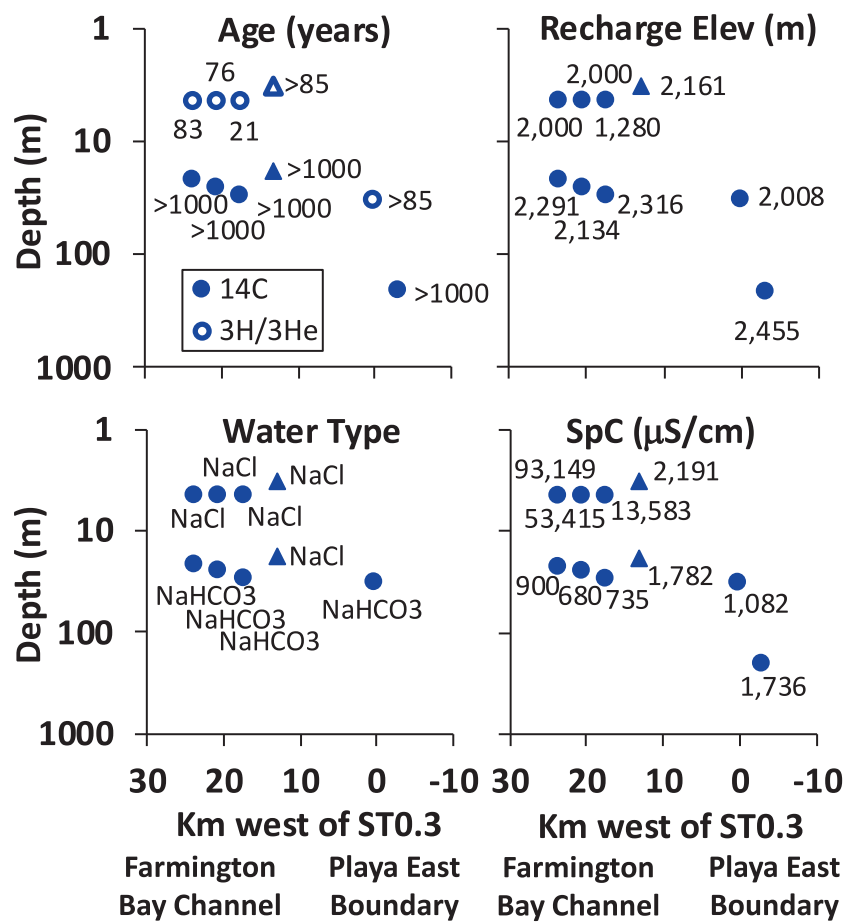


**Fig. 7.** Groundwater age (top left panel), recharge elevation (top right panel), water type (bottom left panel), and SpC (bottom right panel) from selected piezometers within the playa of southeastern GSL (Fig. 1). Circles reflect all piezometers except RS9, which was represented by triangles.

from the “pipe” nature of this feature. Water type was NaCl for shallow groundwater, and NaHCO<sub>3</sub> for deep groundwater (Fig. 7, bottom left panel), wherein the presence of NaHCO<sub>3</sub> rather than CaCO<sub>3</sub> expected for mountain-derived groundwater (Carter, 2025) likely reflects ion exchange during lakeward transport (e.g., Feth et al., 1966). As previously described, SpC decreased dramatically with depth (from hypersaline to fresh), except for round spots, such as site RS9A (center of RS9) which was fresh at all depths (Fig. 7, bottom right panel).

Stable isotope (<sup>2</sup>H/<sup>18</sup>O) signatures demonstrate that most deep groundwater follows the local meteoric water line (LMWL) whereas shallow groundwater displays an evaporative signature (Fig. 8). The water chemistry observations (Figs. 7 and 8) are consistent with a predominant upward flow of ancient mountain-derived groundwater that is mixed and evaporatively concentrated near the ground surface with hypersaline lake water and precipitation/runoff.

Contrasting age, recharge elevation, water type, SpC, and stable isotope signatures between shallow and deep playa groundwater are consistent with the observed predominant upward flow, wherein ancient mountain-derived groundwater slowly flows from depth toward the playa surface, where it mixes with remnant hypersaline (NaCl dominated-high SpC) water and modern precipitation that carry younger age, basin recharge, and evaporative signatures.

#### 4. Discussion

##### 4.1. Fluxes from hydraulic measurements and SpC profiles

That freshwater lies at approximately 9 m depth below the playa surface at discrete locations on the north (AIC) and southeast (ST)

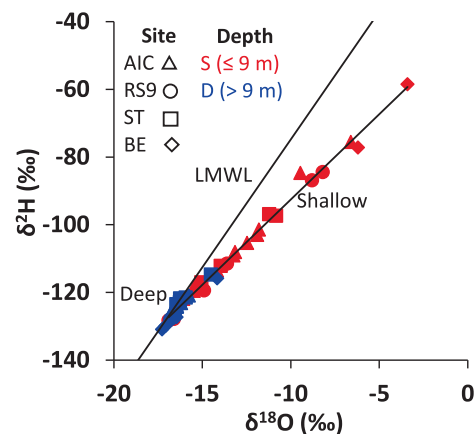


**Fig. 8.** Stable isotope signatures from piezometer and pore water samples within the playa of southeastern GSL (Fig. 1). Sites are shown by symbols. Sample depths (m) are shown for shallow (S, ≤ 9 m) and deep (D, > 9 m) with warm and cool colors, respectively. (For interpretation of the references to colour in this figure legend, the reader is referred to the web version of this article.)

boundaries of Farmington Bay, and at somewhat greater depths at the south shore (BE1) (Fig. 4), as well as at the periphery of round spots in the playa interior (Figs. 5 and 6) suggests that freshwater exists more generally beneath the southern and eastern playa of GSL. Lateral continuity of freshwater at approximately 9 m depth in Farmington Bay is also corroborated by ground-based electrical resistivity measurements

(Michael Thorne, personal communication), and by airborne geophysical measurements (Zhdanov et al., 2026).

The transition with depth from hypersaline to fresh water provides an opportunity to examine the balance of diffusive versus advective flux on the SpC profiles (Fig. 9) to constrain the upward average pore water velocity ( $v$ ) based on an assumed effective molecular diffusion coefficient ( $D_e$ ). Simulation of the salinity profiles was performed using solutions to the 1D advection-dispersion equation:

$$\frac{\partial C}{\partial t} - D_h \frac{\partial^2 C}{\partial x^2} + v \frac{\partial C}{\partial x} = 0 \quad (11)$$

Where  $C$  is the aqueous solute concentration,  $D_h$  is the hydrodynamic dispersion coefficient,  $x$  is the transport distance, and  $t$  is the elapsed time following introduction of the solute. A steady state solution to the above equation for  $C(x)$  is given below in Eq. (12) for the following initial and boundary conditions:

$$C(x, 0) = 0$$

$$C(0, t) = 0$$

$$C(L, t) = C_0 \text{ (source at distance } L\text{)} \text{ where } L \text{ is distance of transport.}$$

$$C(t = \infty) = \frac{C_0 \frac{vx}{e^{D_h t}} - 1}{\left[ \frac{vL}{e^{D_h t}} - 1 \right]} \quad (12)$$

where  $D_h = \alpha v + D_e$ ,  $\alpha$  is the dispersivity of the porous medium, and  $D_e$  is the effective molecular diffusion coefficient in the porous medium.

A transient solution (Ogata and Banks, 1961) to Eq. (11) for  $C(x, t)$  is given in Eq. (13) below for the following initial and boundary conditions:

$$C(x, 0) = 0$$

$$C(0, t) = C_0$$

$$C(\infty, t) = 0$$

$$C(x, t) = \frac{C_0}{2} \left[ \operatorname{erfc} \left\{ \frac{x - vt}{\sqrt[3]{D_h t}} \right\} + \exp \left\{ \frac{vx}{D_h} \right\} \operatorname{erfc} \left\{ \frac{x - vt}{\sqrt[3]{D_h t}} \right\} \right] \quad (13)$$

As stated above, peak salinities occurred at a depth of approximately 3 m, which likely reflects combined effects from surface infiltration, upward flow, periodic lake inundation, and ETr. Whereas, we lack the data needed to account for these temporally variable processes in simulations, we can approximate the system recognizing that the salinity peak occurred at approximately 3 m depth, and background salinity was reached at approximately 15 m depth (Fig. 9), and impose these values

as boundary conditions in Eqs. (12) and (13). At AIC3, the top boundary salinity was 125,000 mg/L, and the background salinity was 1000 mg/L. The effective molecular diffusion coefficient ( $D_e$ ) was set to  $8.94E-10 \text{ m}^2/\text{s}$  based on the geometric mean of a range of values reported for NaCl in clay sediment (Shackelford and Daniel, 1991). The value of dispersivity ( $\alpha$ ) was set to 1.2 m based on the rule of thumb that this value can be taken to be approximately one-tenth of the 12 m transport distance (Gelhar et al., 1992). The upward average pore water velocity at AIC3 ( $v_{est}$ ) was determined to be  $6.8E-3 \text{ m/yr} \pm 3.9E-4 \text{ m/yr}$  from the following equation:

$$v = -K_v^{\text{eff}} \frac{dH}{dL} \frac{1}{\theta} \quad (14)$$

where  $dH/dL$  is the hydraulic gradient, and  $\theta$  is the volumetric water content. At AIC3,  $dH/dL$  between the 3 m and 15 m depth piezometers was  $-8.1E-2 \pm 1.3E-3$ , and a representative volumetric water content of clay sediment was reported to be 0.55 (Woessner and Poeter, 2020).

As shown in Fig. 9 (right panel), the observed salinity profile is explained by Eq. (12) for steady-state conditions when upward velocity was set to a factor-of-two greater than  $v_{est}$ .

We consider this factor-of-two discrepancy to reflect reasonable agreement with our measurements, assuming that the modern salinity profile reflects steady-state conditions. To test this assumption, the Ogata-Banks (1961) transient solution to the advection-dispersion equation was employed, wherein the inlet boundary corresponded to peak salinity at 3 m depth, and the velocity was negative (upward), and the background was 1,000 mg/L. The result shows that the observed salinity profile was matched within a few centuries regardless of the factor-of-two velocity variation around  $v_{est}$  (Figure SI-4). This match confirms that the  $v_{est}$  determined from hydraulic properties explains the observed salinity profile at AIC3, assuming that the value of  $D_e$  is reasonable, and more important, that the observed salinity profile was established over the course of a few centuries, which is a small fraction of the time since GSL assumed its modern regime between 13,000 and 15,000 years ago (Oviatt, 2014).

The above analysis was repeated for site BE1 (Figure SI-5) with top boundary salinity 110,000 mg/L at 6.6 m depth and background salinity 2,400 mg/L at 26.7 m depth, with the same  $D_e$  value as for AIC3 with  $\alpha$  increased to 2 m to reflect the domain size increase to 20 m. The analysis was based on the same  $v_{est}$  as AIC3 assuming equivalent  $K_v^{\text{eff}}$  as AIC3 and noting an equivalent vertical hydraulic gradient to AIC3 (Figure SI-2). The profile at BE1 was explained (Figure SI-5) by an upward velocity

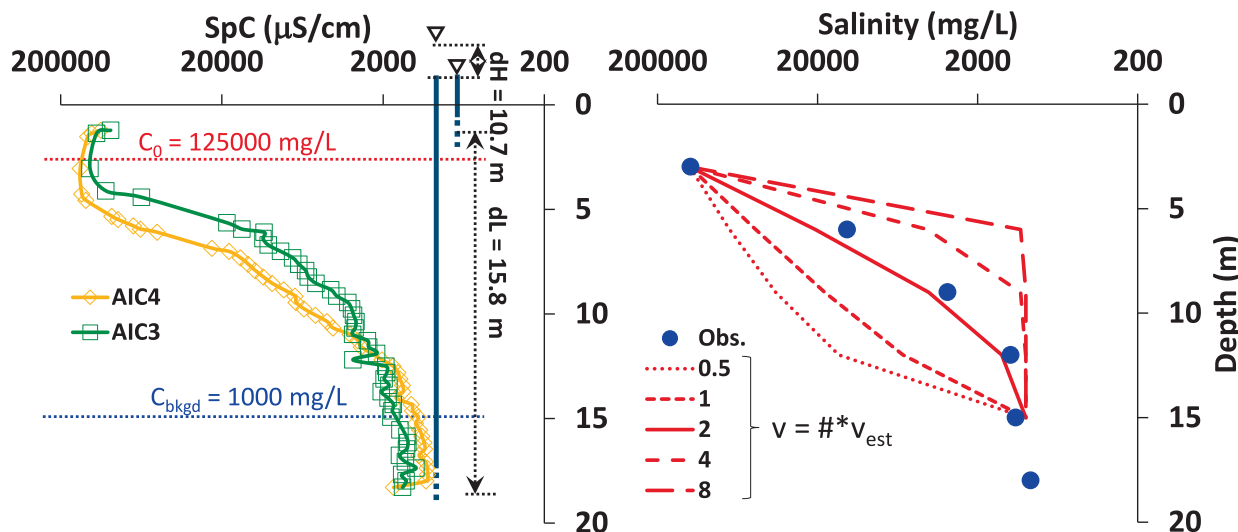


**Fig. 9.** Steady state approach for AIC salinity profile (right panel) showing observed salinity (blue circles) and modeled results for velocities increased by factors-of-two (red lines). Boundary concentrations (red and blue; left panel) correspond to peak and deep salinities in the AIC core salinity profiles (green and gold series). (For interpretation of the references to colour in this figure legend, the reader is referred to the web version of this article.)

that was slightly lower than inferred at AIC3 (e.g., 1.5 times  $v_{est}$ ) and that reached steady state within a millennium at BE1 versus a few centuries at AIC3. However, processes underlying the deeper salinity maximum and higher salinity background at depth at BE1 relative to AIC3 warrant further investigation.

Round spot salinity gradients also constrain estimates of  $K_y^{eff}$ . The  $K_y^{eff}$  for RS9 (1.2E-7 m/s) from laboratory column tests (Fig. 3) is twice the value of  $K_y$  (6.0E-8 m/s) that equates the lateral diffusive flux ( $J_d$ ) to the vertical advective flux ( $J_v$ ) based on boundary conditions set at the edge and intermediate piezometers (Figure SI-6). The value of  $D_e$  used was 8.94E-10 m<sup>2</sup>/s (same as for sites AIC3 and BE1) and the value for  $dH/dL$  was 0.046 (the value at RS9B), which was a factor-of-two above and below the values at RS9C and RS9A, respectively (Figure SI-6). This analysis shows that the higher  $K_y^{eff}$  at RS9 allows local upward flow of freshwater to the playa surface, maintaining a steady state freshwater conduit. As such, the round spots, which are also referred to as “mystery islands” and “phragmites oases” in the press (Larsen, 2025) serve as windows into the underlying ancient artesian groundwater that are opened by the coarser sediment that exist in these locales. Why the sediment is coarser in these locales, and why these features are circular, and whether their existence is related to basement structure, are so far unknown and deserve further investigation.

#### 4.2. Vertical versus lateral specific discharges

The lateral specific discharge across the AIC transect (sites 1 to 4) was determined from the lateral hydraulic gradient between those sites, which was intermediate to the lateral hydraulic gradients for the eastern (higher gradient) and western (lower gradient) segments (Figure SI-3). The measured lateral specific discharge across the AIC transect (1.1E-6 m/day) is approximately seven times lower than the lowest upward vertical specific discharge at AIC4 (7.5E-6 m/day), suggesting that direct groundwater flow from the playa into GSL is limited (Fig. 10). We can make an approximate comparison of vertical to lateral flows by assuming a 3 km-by-3 km map-view area sharing an edge with the corresponding cross-sectional area of flow. Assuming that flow occurs in sediment, and not the underlying bedrock, the maximum depth of lateral flow is 3 km (Zhdanov et al., 2026) constraining a 3 km-by-3 km cross-sectional area of lateral flow. The resulting vertical and lateral flow values (67 and 10 m<sup>3</sup>/day, respectively), each being upscaled from specific discharge by the same area of 9 km<sup>2</sup>, maintains this factor-of-seven ratio of vertical to lateral flows and specific discharges.

The possibility that higher unmeasured lateral flow exists at uncharacterized depths in the circa 3,000 m deep sediments (Zhdanov et al., 2026) is unlikely given the ancient age of the deep playa groundwater. Our findings suggest that groundwater inflow to GSL occurs primarily via seepage into streams and rivers upstream of the playa,

rather than directly from the playa itself, although potential lateral groundwater discharge into GSL at shore locations further west, e.g., microbialite shelves, warrant further investigation.

Vertical groundwater specific discharge was estimated at the AIC transect and RS9 for comparison with evapotranspiration (ETr) rates. Vertical groundwater specific discharges generally decreased westward toward GSL (Fig. 10), with sites AIC4 and AIC3 showing nearly an order of magnitude lower vertical flux relative to AIC1, due predominantly to westward decrease in  $K_y^{eff}$  (Fig. 3). At all sites, except round spots, vertical groundwater specific discharges were two to three orders of magnitude lower than warm season evapotranspiration flux (Fig. 10) reported at the Kaysville-USU Farm Weather Station (Utah Climate Center, Utah State University).

RS9 showed the highest vertical groundwater specific discharge, intermediate to evapotranspiration during the cold and warm seasons (Fig. 10), consistent with observed surface ponding during the cold season, and suggesting that this upward flow is predominantly consumed by evapotranspiration. Upward gradients of multi-millennium aged mountain-derived groundwater below the playa may well contribute to maintenance of soil moisture in the playa. Storage and fluxes within this playa groundwater need further characterization to understand the balance of groundwater and surface water inflows in stabilizing playa soil.

#### 4.3. Contrasting upland versus playa deep groundwater fluxes

Comparison of our results to Carter, 2025 who recently examined the upland groundwater system, demonstrates that upland and playa deep groundwaters are related water types (NaHCO<sub>3</sub> and CaCO<sub>3</sub>), with equivalent SpC (fresh), stable isotope signature (LMWL), and recharge elevation (mountain-derived). The primary distinction is the ancient (multi-millennia) age of the playa groundwater and its predominantly upward flux that contrasts to the multi decade age and large lakeward lateral Darcy flux of the upland groundwater system (approximately 2 m/day) that lies eastward and adjacent to the playa (Carter, 2025). Understanding whether this contrast in age and flow direction is consistent with basin-scale flow requires further investigation, possibly involving greater depths and basin-scale modeling. It is also possible that this contrast in age and flow direction reflects impingement of younger upland lakeward lateral flow upon the ancient upward-moving playa water, which may be the underlying cause of the peripheral wetlands located at the playa-upland boundary (Fig. 1). Additional characterization is needed of the wetland water bodies that exist at the upland-playa transition.

#### 4.4. Implications of the ancient, pressurized, fresh playa groundwater

The ancient, pressurized freshwater below the eastern playa of GSL is clearly a resource that needs further characterization. At minimum this resource may be useful for wetting (dousing) dust hot spots that may increasingly form on the exposed eastern playa as GSL shrinks (Perry et al., 2019), and which pose risk to air quality in proximal metropolitan areas. The confined (pressurized) nature of the groundwater is highly useful, since wherever dust spots may form on the eastern playa, one can install a well, and water will flow to the surface unmechanized under artesian pressure. However, the practicality of inundating playa areas at scales needed for dust source mitigation has not yet been evaluated. Artesian flow from playa wells at depths of 18 m (60 ft) at RS9, 30.5 m (100 ft) at AIC1, and 213 m (700 ft) at PF are all observed to be modest, on the order of 5 L per minute or less, despite two 1.5 m (5 ft) thick pebble gravel layers documented below 122 m (400 ft) in the PF well log. This suggests the need to further characterize the extent to which water can be extracted from this system without negative impacts to the surrounding hydro-ecological system. Future work should also seek to understand the depth to which freshwater extends underneath the eastern playa given that sediments extend to depths of approximately 3,000 m

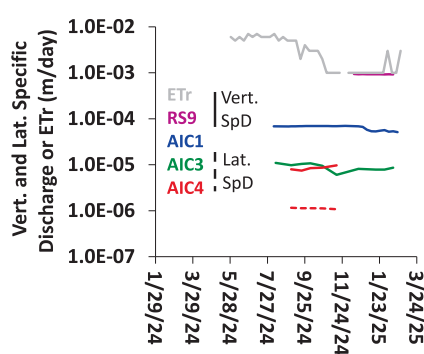


**Fig. 10.** Vertical and lateral specific discharge (SpD) in m/day at AIC sites and RS9 (denoted by color) relative to evapotranspiration (ETr) reported at the Kaysville-USU Farm Weather Station (Utah Climate Center, Utah State University). The vertical and lateral specific discharges are denoted by solid and dash lines, respectively.

(10,000 ft) (e.g., Zhdanov et al., 2026).

Because terminal lakes occur in regional hydrologic basins, the occurrence of pressurized groundwater on their peripheries may be common phenomena. Similarities between lake Urmia of Iran and Great Salt Lake in terms of size, setting, and challenges, are well described (Wurtsbaugh and Sima, 2022). As literature accumulates, it will be useful to assess the similarities and contrasts among playa groundwater characteristics across terminal lakes globally, and to assess whether similar strategies emerge to mitigate the impacts of dust from exposed playa. Protocols designed to increase flow to GSL have to date assumed that groundwater under the playa is effectively part of the lake. Our finding is that the reality is not so straightforward. The relative effectiveness of options by which existing water rights under the playa can contribute water to GSL (e.g., via non-use versus pump and conveyance to GSL) warrant further consideration.

### CRediT authorship contribution statement

**Ebenezer Adomako-Mensah:** Writing – review & editing, Writing – original draft, Visualization, Validation, Methodology, Investigation, Formal analysis, Data curation, Conceptualization. **William P. Johnson:** Writing – review & editing, Writing – original draft, Visualization, Validation, Supervision, Resources, Project administration, Methodology, Investigation, Funding acquisition, Formal analysis, Data curation, Conceptualization. **Samuel C. Carter:** Writing – review & editing, Methodology, Investigation, Data curation. **D. Kip Solomon:** Writing – review & editing, Supervision, Resources, Methodology, Investigation, Data curation. **William D. Mace:** Resources, Methodology. **Scott A. Hynek:** Resources, Methodology, Investigation. **Hugh Hurlow:** Writing – review & editing, Supervision, Resources, Methodology, Investigation, Data curation.

### Declaration of competing interest

The authors declare that they have no known competing financial interests or personal relationships that could have appeared to influence the work reported in this paper.

### Acknowledgements

This material is based upon work supported by grants from the Utah Division of Forestry, Fire and State Lands (FFSL) of the Utah Department of Natural Resources and the Great Salt Lake Commissioners Office. Any opinions, findings, and conclusions or recommendations expressed in this material are those of the authors and do not necessarily reflect the views of these funding sources.

### Appendix A. Supplementary data

Supplementary data to this article can be found online at <https://doi.org/10.1016/j.jhydrol.2025.134813>.

### Data availability

Data spreadsheets (Excel) are available at the following: Adomako-Mensah, E. (2025). AdomakoetalJHyd2025-SI, HydroShare, <http://www.hydroshare.org/resource/8dda2368a62c40e194088d74a69f497b>.

### References

- Adomako-Mensah, E., 2025. Significance of Ancient Artesian Fresh Groundwater Below The Playa of a Hypersaline Terminal Lake of Hemispheric Significance [master's thesis]. University of Utah.
- Aschbach-Hertig, W., Solomon, D.K., 2013. Noble gas thermometry in groundwater hydrology. In: Burnard, P. (Ed.), The Noble Gases as Geochemical Tracers. Springer, Berlin, pp. 81–122. [https://doi.org/10.1007/978-3-642-28836-4\\_5](https://doi.org/10.1007/978-3-642-28836-4_5).
- Bowen, G.J., Putman, A., Brooks, J.R., Bowling, D.R., Oerter, E.J., Good, S.P., 2018. Inferring the source of evaporated waters using stable H and O isotopes. *Oecologia* 187 (4), 1025–1039. <https://doi.org/10.1007/s00442-018-4192-5>.
- Brooks, P.D., Gelderloos, A., Wolf, M.A., Jamison, L.R., Strong, C., Solomon, D.K., Bowen, G.J., Burian, S., Tai, X., Arens, S., Briefer, L., Kirkham, T., Stewart, J., 2021. Groundwater-mediated memory of past climate controls water yield in snowmelt-dominated catchments. *Water Resour. Res.* 57 (10), e2021WR030605. <https://doi.org/10.1029/2021WR030605>.
- Bunce, L.E., Lowenstein, T.K., Jagnecki, E., Collins, D., 2025. Significance of Spring Inflow to Great Salt Lake, Utah, U.S.A. *Hydrology* 12 (159). <https://doi.org/10.3390/hydrology12060159>.
- Carter, S.C., 2025. Using environmental tracers to develop a conceptual framework of groundwater inflow into Farmington Bay, Great Salt Lake, UT [master's thesis]. University of Utah. <https://collections.lib.utah.edu/ark:/87278/s61sr411>.
- Conover, M.R., Bell, M.E., 2020. Importance of Great Salt Lake to pelagic birds: eared grebes, phalaropes, gulls, ducks, and white pelicans. In: Baxter, B.K., Butler, J.K. (Eds.), Great Salt Lake Biology: A Terminal Lake in a Time of Change. Springer, pp. 239–262. [https://doi.org/10.1007/978-3-030-40352-2\\_8](https://doi.org/10.1007/978-3-030-40352-2_8).
- Eutech Instruments, 1997. Conductivity to TDS conversion factors. <http://www.eutechinst.com/tips/contds/07.pdf> (Accessed 20 August 2025).
- Feth, J.H.F., Barker, D.A., Moore, L.G., Brown, R.J., Veirs, C.E., 1966. Lake Bonneville: geology and hydrology of the Weber Delta district, including Ogden, Utah. *Prof. Paper Rep.* 518, 86. <https://doi.org/10.3133/pp518>.
- Gardner, P.M., Heilweil, V.M., 2014. A multiple-tracer approach to understanding regional groundwater flow in the Snake Valley area of the eastern Great Basin, USA. *Appl. Geochem.* 45, 33–49. <https://doi.org/10.1016/j.apgeochem.2014.02.010>.
- Gelhar, L.W., Welty, C., Rehfeldt, K.R., 1992. A critical review of data on field-scale dispersion in aquifers. *Water Resour. Res.* 28 (7), 1955–1974. <https://doi.org/10.1029/92WR00607>.
- Gillespie, J., Nelson, S.T., Mayo, A.L., Tingey, D.G., 2012. Why conceptual groundwater flow models matter: a trans-boundary example from the arid Great Basin, western USA. *Hydrogeol. J.* 20, 1133–1147. <https://doi.org/10.1007/s10040-012-0848-0>.
- Godfrey, S.E., Kirchner, J.W., Clow, D.W., 2009. Concentration-discharge relationships reflect chemostatic characteristics of US catchments. *Hydrolog. Process.* 23 (13), 1844–1864. <https://doi.org/10.1002/hyp.7315>.
- Great Salt Lake Strike Team, 2025. Great Salt Lake data and insights summary. A synthesized resource document for the 2025 General Legislative Session. <https://d36oiw74r1rap.cloudfront.net/wp-content/uploads/2025/01/GSL-Jan2025.pdf> (Accessed 25 August 2025).
- Grineski, S.E., Mallia, D.V., Collins, T.W., Araos, M., Lin, J.C., Anderegg, W.R.L., Perry, K., 2024. Harmful dust from drying lakes: preserving Great Salt Lake (USA) water levels decreases ambient dust and racial disparities in population exposure. *One Earth* 7 (6), 1056–1067. <https://doi.org/10.1016/j.oneear.2024.05.006>.
- Gu, H., Zhang, W., Gillies, R., 2024. The shrinking Great Salt Lake may exacerbate droughts by reducing local precipitation: a case study. *J. Hydrometeorol.* 25 (7), 1099–1109. <https://doi.org/10.1175/JHM-D-23-0189.1>.
- Hall, D.K., O'Leary, D.S., DiGirolamo, N.E., Miller, W., Kang, D.H., 2021. The role of declining snow cover in the desiccation of the Great Salt Lake, Utah, using MODIS data. *Remote Sens. Environ.* 252, 112106. <https://doi.org/10.1016/j.rse.2020.112106>.
- Hassibe, W.R., Keck, W.G., 1991. The Great Salt Lake. *U.S. Geol. Surv. Gen. Inform. Product* 25. <https://doi.org/10.3133/70039229>.
- Hem, J.D., 1985. Study and interpretation of the chemical characteristics of natural water. In: U.S. Geological Survey Water Supply Paper 2254, p. 263 <https://pubs.usgs.gov/publication/wsp2254> (Accessed 20 August 2025).
- Herring, G., Whipple, A.L., Aldridge, C.L., Pulver, B.A., Eagles-Smith, C.A., Inman, R.D., Matchett, E.L., Monroe, A.P., Orning, E.K., Robb, B.S., Shyvers, J.E., Tarbox, B.C., Van Schmidt, N.D., Smith, C.D., Holloran, M.J., Overton, C.T., O'Leary, D.R., Casazza, M.L., Frus, R.J., 2024. Imperiled Great Basin terminal lakes: synthesizing ecological and hydrological science gaps and research needs for waterbird conservation. *Bioscience* 75, 112–126. <https://doi.org/10.1093/biosci/biae126>.
- Hvorslev, M., 1951. Time lag and soil permeability in ground-water observations. U.S. Army Engineer Waterways Experiment Station Bulletin No. 36. Accessed 15 May 2025. <https://hdl.handle.net/11681/4796>.
- Johnson, W.P., Wurtsbaugh, W.A., Belovsky, G.E., Baxter, B.K., Black, F., Angeroth, C., Jewell, P., Yang, S., 2019. Geochemistry of Great Salt Lake. In: Maurice, P.A. (Ed.), Encyclopedia of Water: Science, Technology and Society. John Wiley and Sons Inc., Hoboken, NJ <https://doi.org/10.1002/9781119300762.wst0072>.
- Jones, B.F., Naftz, D.L., Spencer, R.J., Oviatt, C.G., 2009. Geochemical evolution of Great Salt Lake, Utah, USA. *Aquat. Geochem.* 15 (1), 95–121. <https://doi.org/10.1007/s10498-008-9047-y>.
- Larsen, L., 2025. A solution to the Great Salt Lake's blowing dust might lie deep beneath its surface: The Salt Lake Tribune. <https://www.sltrib.com/news/environment/2025/07/03/water-beneath-great-salt-lake> (Accessed 10 August 2025).
- Lowe, M., 2003. The Weber River Basin aquifer storage and recovery project. *Utah Geol. Surv.* <https://doi.org/10.34191/OFR-419>.
- Manning, A.H., Solomon, D.K., 2004. Constraining mountain-block recharge to the Eastern Salt Lake Valley, Utah with dissolved noble gas and tritium data. In: Hogan, J.F., Phillips, F.M., Scanlon, B.R. (Eds.), Groundwater Recharge in a Desert Environment, The Southwestern United States. <https://doi.org/10.1029/009WSA09>.
- Masbruch, M.D., Rumsey, C.A., Gangopadhyay, S., Susong, D.D., Pruitt, T., 2016. Analyses of infrequent (quasi-decadal) large groundwater recharge events in the northern Great Basin: their importance for groundwater availability, use, and management. *Water Resour. Res.* 52 (10), 7819–7836. <https://doi.org/10.1002/2016WR019060>.

- Mayo, A.L., Klauk, R.H., 1991. Contributions to the solute and isotopic groundwater geochemistry, Antelope Island, Great Salt Lake, Utah. *J. Hydrol.* 127, 307–335. [https://doi.org/10.1016/0022-1694\(91\)90120-7](https://doi.org/10.1016/0022-1694(91)90120-7).
- Michel, R.L., Jurgens, B.C., Young, M.B., 2018. Tritium deposition in precipitation in the United States, 1953–2012. In: U.S. Geological Survey Scientific Investigations Report 2018-5086, p. 28 <https://pubs.usgs.gov/sir/2018/5086/sir20185086.pdf>.
- Ogata, A., Banks, R.B., 1961. A solution of the differential equation of longitudinal dispersion in porous media. In: U.S. Geological Survey Professional Paper 411-A, pp. A1–A7. <https://doi.org/10.3133/pp411A>.
- Oviatt, C.G., 2014. The Gilbert Episode in the Great Salt Lake Basin, Utah. Utah Geological Survey miscellaneous Publication, p. 20. <https://doi.org/10.34191/mp-14-3>.
- Perry, K.D., Crozman, E.T., Hoch, S.W., 2019. (Unpublished results). Results of the Great Salt Lake dust plume study (2016–2018), final report. Department of Atmospheric Sciences. University of Utah, Salt Lake City, UT.
- Ponce, V.M., 2014. Total dissolved solids based on electrical conductivity: Online salinity calculator. <http://ponce.sdsu.edu/onlinesalinity.php> (Accessed 15 August 2025).
- Post, V.E.A., Simmons, C.T., 2021. Variable-density groundwater flow. In: The Groundwater Project, Guelph, Ontario, Canada. <https://doi.org/10.21083/978-1-77470-046-4>.
- Rice, E.W., Baird, R.B., Eaton, A.D. (Eds.), 2017. Standard Methods for the Examination of Water and Wastewater (23rd ed., Section 2520 C). American Public Health Association, American Water Works Association and Water Environment Federation, Washington, DC. <https://doi.org/10.2105/SMW2.2882.028>.
- Shackelford, C.D., Daniel, D.E., 1991. Diffusion in saturated soil II: results for compacted clay. *J. Geotech. Eng.* 117 (3), 485–506. [https://doi.org/10.1061/\(ASCE\)0733-9410\(1991\)117:3\(485\)](https://doi.org/10.1061/(ASCE)0733-9410(1991)117:3(485)).
- Tavernia, B.G., Meehan, T., Neill, J., Luft, J., 2021. Hydrology affects shorebirds, waterfowl, and other waterbirds at Bear River Bay, a globally important bird area. *J. Field Ornithol.* 92, 388–401. <https://doi.org/10.1111/jfo.12381>.
- Thiros, S.A., Bexfield, L.M., Anning, D.W., Huntington, J.M., 2010. Conceptual understanding and groundwater quality of selected basin-fill aquifers in the Southwestern United States. In: U.S. Geological Survey Professional Paper 1781, Reston, Virginia. <https://doi.org/10.3133/pp1781>.
- Thiros, S.A., Manning, A.H., 2004. Quality and sources of ground water used for public supply in Salt Lake Valley, Salt Lake County, Utah, 2001. U.S. Geological Survey Water Resources Investigations Report 03-4325 doi:10.3133/wri034325.
- Waddell, K.M., Barton, J.D., 1980. Estimated inflow and evaporation for Great Salt Lake, Utah, 1931–76, with revised model for evaluating the effects of dikes on the water and salt balance of the lake: comprehensive water planning program. Cooperative Investigations Report No. 20. Utah Department of Natural Resources <https://pubs.usgs.gov/publication/70046184>.
- Water Quality Portal, 2021. Washington (DC), National Water Quality Monitoring Council, United States Geological Survey (USGS), Environmental Protection Agency (EPA). doi:10.5066/P9QRKUVJ.
- Wilson, R.M., 2010. Seeking refuge: birds and landscapes of the pacific flyway. *Environ. History* 16 (3), 553–554. <https://doi.org/10.1093/envhis/emr069>.
- Woessner, W.W., Poeter, E.P., 2020. Hydrogeologic properties of earth materials and principles of groundwater flow. In: The Groundwater Project. <https://doi.org/10.21083/978-1-7770541-2-0>.
- Wolf, M.A., Jamison, L.R., Solomon, D.K., Strong, S., Brooks, P.D., 2023. Multi-year climatic controls on groundwater storage in seasonally snow-covered headwater catchments. *Water Resour. Res.* 59 (4), e2022WR033394. <https://doi.org/10.1029/2022WR033394>.
- Wurtsbaugh, W.A., Sima, S., 2022. Contrasting management and fates of two sister lakes: Great Salt Lake (USA) and Lake Urmia (Iran). *Water* 14 (19), 3005. <https://doi.org/10.3390/w14193005>.
- Wurtsbaugh, W.A., Miller, C., Null, S.E., DeRose, R.J., Wilcock, P., Hahnberger, M., Howe, F., Moore, J., 2017. Decline of the world's saline lakes. *Nat. Geosci.* 10, 816–821. <https://doi.org/10.1038/ngeo3052>.
- Wurtsbaugh, W.A., Miller, C., Null, S.E., Wilcock, P., Hahnberger, M., Howe, F., 2016. Impacts of water development on Great Salt Lake and the Wasatch Front. In: Watershed Sciences Faculty Publications, Paper 875. <https://doi.org/10.13140/RG.2.1.4196.3284>.
- Zamora, H., Inkenbrandt, P., 2024. Estimate of groundwater flow and salinity contribution to the Great Salt Lake using groundwater levels and spatial analysis. *Utah Geol. Assoc. Publ.* 51, 24 p. <https://doi.org/10.31711/ugap.v51.i141>.
- Zhdanov, M. S., Jorgensen, M., Cox L., Johnson, W.P., Solomon, D.K., 2026, Airborne Geophysical Imaging of a Potential Freshwater Reservoir Beneath the Great Salt Lake, in review.

## Glossary

**Term:** Definition

**Specific conductivity ( $SpC$ ):** A measure of water's ability to conduct electrical current, normalized to 25 °C

**Hydraulic Conductivity ( $K$ ):** The proportionality constant in Darcy's Law that describes the relative ease with which a fluid can move through a porous material under a hydraulic gradient. It depends on both the properties of the fluid and the pore structure of the medium

**Horizontal hydraulic conductivity ( $K_h$ ):** The hydraulic conductivity representing the ease of groundwater flow in the horizontal direction

**Vertical hydraulic conductivity ( $K_v$ ):** The hydraulic conductivity representing the ease of groundwater flow in the vertical direction

**Effective (thickness-weighted harmonic mean) vertical hydraulic conductivity ( $K_v^{eff}$ ):** An equivalent vertical conductivity for heterogeneous media, calculated using the thickness-weighted harmonic mean to account for flow across stratified units

**Effective (thickness-weighted geometric mean) horizontal hydraulic conductivity ( $K_h^{eff}$ ):** An equivalent horizontal conductivity for heterogeneous media, calculated using the thickness-weighted geometric mean to account for lateral flow through stratified units

**Mid-screen elevation ( $z_s$ ):** The elevation at the midpoint of a screened interval in a well, used to approximate the hydraulic head measurement depth.

**Hydraulic gradient ( $dH/dL$ ):** The change in hydraulic head per unit distance in the direction of groundwater flow

**Evapotranspiration ( $ET_r$ ):** The combined water loss to the atmosphere through soil evaporation and plant transpiration under reference crop conditions